Petroleum Science
https://doi.org/10.1007/s12182-020-00532-z

ORIGINAL PAPER

# Effect of anodic dissolution and passivation on X80 steel in $NaHCO_3$ solution

**Lai-Shun Yang[1,3] · Chao Yang[2,3]**

Received: 28 February 2020 / Accepted: 14 September 2020


**Abstract**
The effects of extreme stray current on the anodic dissolution and passivation of X80 steel in $NaHCO_3$ solution were investigated using measurements of polarization curves and EIS, AFM and SEM techniques. Under the interference of anodic current ($i = 0$~$200$ A/m$^2$), main constituents of corrosion products of X80 steel were FeO(OH) and $Fe_3O_4$. A double-layer film formed at $i = 100$ A/m$^2$, in which FeOOH was in outer and $Fe_3O_4$ lied in inner. The formation mechanism of $Fe_3O_4$ was confirmed and described by the electrochemical reaction in various regions on anodic potentiodynamic polarization curve.

**Keywords** Anodic current · Passivation · X80 steel · $Fe_3O_4$ · Near-neutral solution

## 1 Introduction

In recent years, considerable attention has been paid to metal corrosion (Li et al. 2015). Buried pipelines have been spotlighted to be protected by combination of coatings (Cui et al. 2017; Prasai et al. 2012) and cathodic protection (Refait et al. 2015). Even though this method is widely considered to be sufficiently effective, stray current makes it impossible to pipeline away from corrosion, especially in which there are some defects on coatings. Numerous efforts (Chen et al. 2017; Jadhav and Gelling 2019) have been made to investigate the corrosion process of steel, as well as the corrosion products, and stray current is caught more attention due to its surprisingly critical corrosion rate.

Compared to direct stray current (DC), more literature focuses on its corrosion rate, product, mechanism and model of alternating stray current (AC), and a comprehensive understanding has been in consensus (Xu et al. 2012). However, based on the regulation that DC corrosion rate conforms to Faraday's law, few researches have been conducted on its corrosion behavior, even though corrosion rate resulted by DC is much larger than that of AC. Furthermore, corrosion becomes more severely with the development of HVDC (High Voltage Direct Current), which current flowing into soil can reach thousands of amperes once this system runs in fault (Nicholson 2010). The results we got preliminary based on simulation and field test show the peak of current density at defects on coatings can reach 150 A/m$^2$, which may cause the rapid perforation of pipeline (Yang et al. 2019). It is interesting that at some points current flows out into soil, the surface of defects is covered with a layer of dense products, which prevents the later soil corrosion. However, this issue has not been addressed with as much fervor.

The above phenomenon is mostly consistent with the characteristic of anodic passivation theory (Ejaz et al. 2015). However, detailed descriptions are impossible. It has to be admitted that in many fields, research on passivated metal system (Wang et al. 2015) is in full bloom, such as super stainless steel (Tranchida et al. 2018; Xu et al. 2015), high entropy alloy (Cui et al. 2019), etc., while anodic passivation is continuously concerned to be strongly avoided in few field, i.e., metal's electrolysis and battery.

Moreover, the research on carbon steel and high-strength steel points out that anode passivation membrane is consisted of $Fe_2O_3$ and $Fe_3O_4$. From the other perspective of

Edited by Xiu-Qiu Peng

✉ Chao Yang
yangchao201001@163.com

[1] College of Civil Engineering and Architecture, Shandong University of Science and Technology, Qingdao 266590, Shandong, China

[2] Technology Inspection Center of Shengli Oilfield, SINOPEC, Dongying 257000, Shandong, China

[3] China University of Petroleum (East China), Qingdao 266580, Shandong, China

Published online: 01 December 2020

passivation environment, the strong oxidizing acid such as concentrated sulfuric acid and nitric acid is focused on, while passivation behavior in alkaline environment is rarely studied due to its harsh conditions, i.e., $NO_3^-$. The passivation problem in metal electroplating process is similar to the research background of this paper. However, considering the economy of electroplating, the applied anodic current density is generally less than 10 A/m$^2$, which is much smaller than the range of anodic current density to be studied. Under this circumstance, relevant scholars generally believe that the main way to eliminate the passivation in electroplating is to increase the applied anodic current density, that is, the metal will not be passivated under a larger anodic current density, which is obviously contrary to the phenomena mentioned in this paper.

Therefore, there are two challenges in elucidating the metal's corrosion behavior interference by lager anodic current: (1) a deeper insight needs to be put forward for corrosion behavior and process due to DC stray current, and (2) related parameters of anodic passivation should be determined.

In this work, we introduced anodic current interference (0 ~ 200 A/m$^2$) into the electrochemical test system for X80 steel in 3 wt% $NaHCO_3$ solution. The polarization curves and electrochemical impedance spectrum were conducted to determine corrosion kinetic parameters under the interference of anodic current, and combining with characterization of corrosion products, anodic passivation process was also illustrated. The results can provide a clear explanation for anodic dissolution and corrosion process caused by a larger direct current in near-neutral solution.

## 2 Experimental section

Figure 1 shows the experimental device of electrochemical test of X80 steel in 3 wt% $NaHCO_3$ solution under different anodic current densities. DC power and electrochemical testing system were installed in two devices, respectively, to reduce the influence of the anode electric field on the test results. The anodic current applied on X80 steel was conducted by platinum electrode and determined by ampere meter. Conventional three-electrode system was used for electrochemical test, X80 steel as working electrode, Pt as auxiliary electrode and SCE as reference electrode. The reference electrode was positioned sufficiently close to the electrode surface of less than 2 mm. Thus, the effect of ohmic drop on the potential measurement was negligible (Liang et al. 2018).

Working electrodes used in this work were fabricated from a sheet of X80 steel (mass fraction in %: C 0.063, Si 0.28, Mn 1.83, P 0.011, S 0.0006, Cr 0.03, Ni 0.03, Ti 0.016, Nb 0.061, V 0.059, Mo 0.22 and Fe in balance). The steel coupons were manufactured into 25 × 25 × 2 mm$^3$ cubes that fringe effect was ignored, and were embedded in epoxy resin, leaving a working area of 6.25 cm$^2$. Specimen preparation was controlled carefully to ensure that there was no groove and bubble generating at the epoxy/steel interface. The working surface of the specimen was subsequently ground with 800 grit and 1000 grit sand papers and cleaned by distilled water and methanol, then standby application after dry.

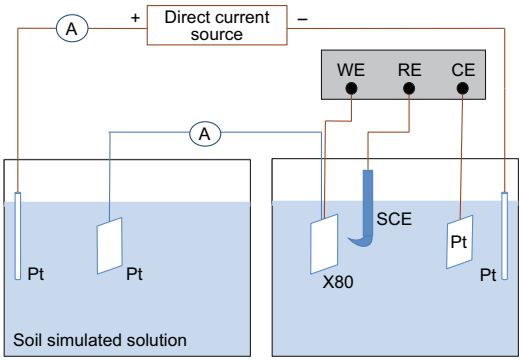


**Fig. 1** Experimental device of electrochemical test of X80 steel in 3 wt% $NaHCO_3$ solution under different anodic current densities

Considering the soil properties in field ($HCO_3^-$, $Cl^-$, $Ca^{2+}$, $Na^+$, $K^+$ and $Mg^{2+}$) of pH = 7.4–8.5, the experimental solution was prepared by Analytical Pure $NaHCO_3$ and deionized water with pH = 8.168 at 25℃.

In this paper, three groups of electrochemical tests are designed. A group test including three electrochemical experiments was carried out in order. Firstly, OCP test lasted for long time to determine the system in a stable state. The average of OCP and error analysis were added in this paper. Secondly, in a stable stage, the Tafel polarization curves in different anodic current densities were tested to obtain the dynamic parameters. Thirdly, for another stable stage, the EIS curves were tested.

Tafel polarization curves were measured by electrochemical working station (PARSTAT 2273) at a potential scanning rate of 0.3 mV/s in the range of ± 250 $mV_{vs.OCP}$ (SCE), and electrochemical impedance spectrum was tested from the application of the alternating current signal (10 mV) with the frequency from $10^5$ to $10^{-2}$ Hz. All experiments were carried out in constant temperature humidity chamber (GDJS-408) at temperature 25℃. The electrochemical parameters were obtained by commercial software of "PowerSuite" and "ZSimpWin" software.

## 3 Result and discussion

### 3.1 Open circuit potential ($E_{OCP}$)

Considering the larger corrosion rate caused by anodic current density (*i*-ACD), the open-circuit potential ($E_{OCP}$) of X80 steel was tested after immersion in different anodic current densities for 10 mins. When the $E_{OCP}$ fluctuated no more than 5 mV in at least 300 s, it was considered that the whole system reached a stable state and further polarization curve and electrochemical impedance could be carried out. Experiments were carried out for three times under different anodic current densities, and the $E_{OCP}$ with standard deviation ($\sigma$) after stabilization is shown in Fig. 2.

Compared with the $E_{OCP}$ without *i*-ACD, when the applied *i*-ACD was 50 A/m$^2$, the $E_{OCP}$ shifted sharply from − 804.95 mV to − 72.03 mV. As *i*-ACD continued to increase, the $E_{OCP}$ generally moved to be more positive, indicating that the corrosion tendency of X80 steel increased with the increase in the anodic current density. However, when *i*-ACD was 100 A/m$^2$, the $E_{OCP}$ shifted negatively from − 3.93 mV to − 131.04 mV, meaning a decreasing corrosion tendency. Therefore, the following section will focus on the polarization curve, electrochemical impedance and image characterization to explore the causes of the phenomenon.

### 3.2 Tafel polarization curves

Figure 3 presents the Tafel polarization curves of X80 steel with the influenced by the anodic current densities at $i$=0~200 A/m$^2$ in 3 wt% $NaHCO_3$ solution, from which the corrosion potential ($E_{corr}$), corrosion current density ($I_{corr}$),

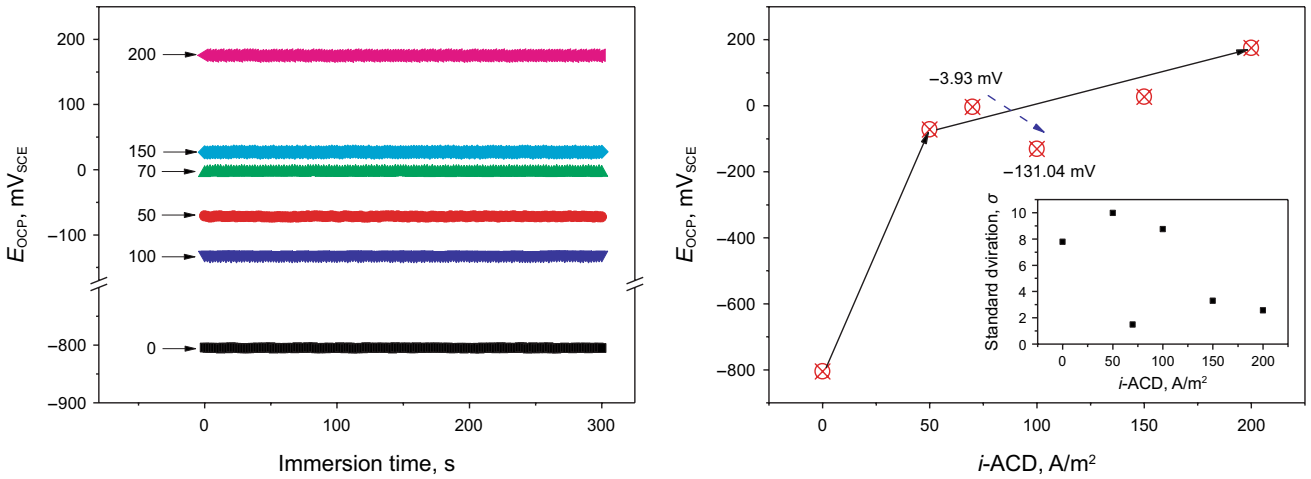


**Fig. 2** Open circuit potential of X80 steel at $i$=0–200 A/m$^2$

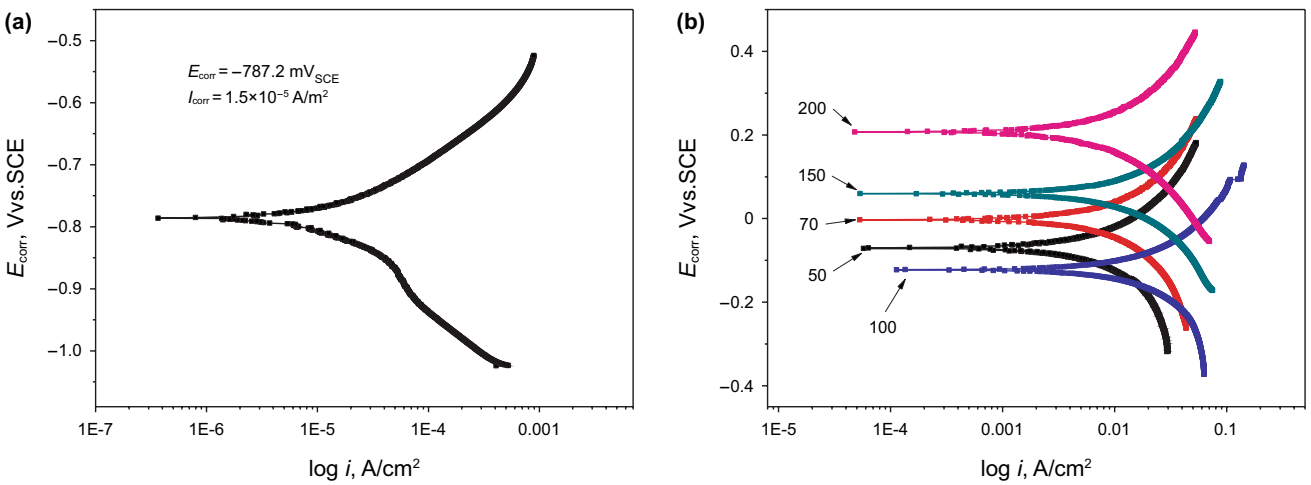


**Fig. 3** Tafel polarization curves of X80 steel at $i$=0–200 A/m$^2$

anodic- and cathodic-Tafel slop ($\beta_a$, $\beta_c$) were determined, as shown in Table 1.

Different from $E_{OCP}$ (open circuit potential), the measurement of $E_{corr}$ was free of influence by the electrical resistance of corrosion product and, thus, more accurately reflected the corrosion conditions of the X80 steel (Philippe et al. 2008). The $E_{corr}$ of the steels influenced by anodic current at $i$=0~200 A/m$^2$ were − 787.16, − 70.06, − 2.46, − 122.31, 30.31 and 207.60 mV, respectively, indicating that the $E_{corr}$ generally increased caused by anodic polarization with the increase of $i$-ACD. However, the $E_{corr}$ of the steel at $i$=100 A/m$^2$ was significantly less negative than that of the others, showing a better protection at $i$=100 A/m$^2$.

The outstanding corrosion performance of $i$-ACD was confirmed by the $I_{corr}$ data (corrosion current density) of influenced steels. The steel influenced by $i$-ACD exhibited the greatest $I_{corr}$ 4 or 5 orders of magnitude higher than the steel without $i$-ACD ($I_{corr\text{-}0}=1.5\times10^{-3}$ μA/m$^2$). The $I_{corr}$ generally increased with the increase of $i$-ACD. Compared to the $I_{corr\text{-}0}$ ($1.5\times10^{-3}$ μA/m$^2$), indicating the corrosion current density at $i$=0, within the scope of investigating $i$=0~200 A/m$^2$, the $I_{corr}$ reached maximum at $i$=200 A/m$^2$, which increased by $8\times10^4$ %. Moreover, there was a substantial shift of the $I_{corr}$ from $i$=70 A/m$^2$ to $i$=100 A/m$^2$ ($I_{corr\text{-}100}<I_{corr\text{-}70}$), even the $I_{corr\text{-}50}$ was about equal to $I_{corr\text{-}100}$, while $I_{corr\text{-}150}$ was approximately three times greater than $I_{corr\text{-}100}$, confirming that the corrosion-product layer formed at $i$=100 A/m$^2$ played the most crucial role in enhancing the corrosion resistance than the others. Note that the $I_{corr}$ data obtained from the Tafel polarization curves of steel consisted of two components: the corrosion reaction on the surface of steel and the diffusion process of corrosion product between steel and electrolyte. While it was impossible to differentiate their contribution to $I_{corr}$, these two processes will be discussed in the results of electrochemical impedance spectroscopy (EIS) measurements.

The anodic- and cathodic-Tafel constants, named as $\beta_a$ and $\beta_c$, respectively, can reflect the polarization degree. Due to the anodic polarization, the $\beta_a$ generally increased while $\beta_c$ decreased as $i$-ACD increased, representing that the ratio of $\beta_a$ and $\beta_c$ ($r=\beta_a/\beta_c$) was almost more than 1. However, at $i$=100A/m$^2$, the $\beta_a$ reached the minimum of 665 and $\beta_c$ was 1495 in maximum, so as the $r$=0.447 < 1, indicating the $I_{corr}$ decreased, which met the analysis of $E_{corr}$.

### 3.3 Anodic passivation mechanism

To explore the mysterious phenomenon of $E_{corr}$ and $I_{corr}$ decreasing at $i$=100 A/m$^2$, the immersion experiment was carried out in 3 wt% $NaHCO_3$ solution. The four groups of experiments were set up in different immersion time of 10 min, 20 min, 30 min and 1 h, respectively. The loose corrosion product was clean out using standard derusting fluid, and then, the corrosion morphology of dense corrosion-product layer was analyzed by AFM and SEM.

The changing morphology of dense corrosion-product is shown in Fig. 4. After immersing 10 min, there was still black and insoluble corrosion product on the treated surface, obtained from the AFM as shown in Fig. 4a. The surface of X80 steel was partly covered with disordered granular corrosion products, and the corrosion products presented obvious dispersion. As immersion time reached 20 min, the particle size of corrosion product on the surface gradually increased. In the observed area, a thin film of corrosion products was basically formed to cover the whole sample. And small corrosion-product particles were agglomerated to form larger groups.

As immersion time lasted to 30 min, it could be seen from Fig. 4d of the unbroken corrosion products, which were divided into two distinct layers: the yellow and loose corrosion-product layer and the black and dense corrosion-product layer. In order to determine the composition of the corrosion products of the two layers, the particle morphology was observed. The structure in outer layer presented the rhombic, identified as α-FeO(OH) and γ-FeO(OH) (Zhang et al. 2018; Raman et al. 1989). Meanwhile, the inner layer with the characteristic of dense and black illustrated a tapered regular hexahedron, which meant its component was $Fe_3O_4$ (Tanaka et al. 2014).

The growth of inner corrosion products was observed by AFM with time. At 30 min (Fig. 4c), $Fe_3O_4$ particles further clustered together to form larger particles, which can be demonstrated by the height contrast in different AFM figures. Moreover, the thickness and inhomogeneity

**Table 1** Fitted results of Tafel polarization curves of X80 steel at $i$=0~200 A/m$^2$

| $i$-ACD, A/m$^2$ | $E_{corr}$, mV$_{SCE}$ | $I_{corr}$, μA/m$^2$ | $\beta_a$, mV/decade | $\beta_c$, mV/decade | $r=\beta_a/\beta_c$ |
|---|---|---|---|---|---|
| 0 | − 787.16 | $1.51\times10^{-3}$ | 146.80 | 107.98 | 1.36 |
| 50 | − 70.06 | 35.30 | 998.78 | 721.99 | 1.38 |
| 70 | − 2.46 | 52.57 | 1299.39 | 849.55 | 1.53 |
| 100 | − 122.31 | 35.75 | 665.60 | 1495.75 | 0.44 |
| 150 | 30.31 | 93.37 | 1486.98 | 1198.97 | 1.24 |
| 200 | 207.60 | 120.50 | 7679.82 | 627.30 | 12.24 |

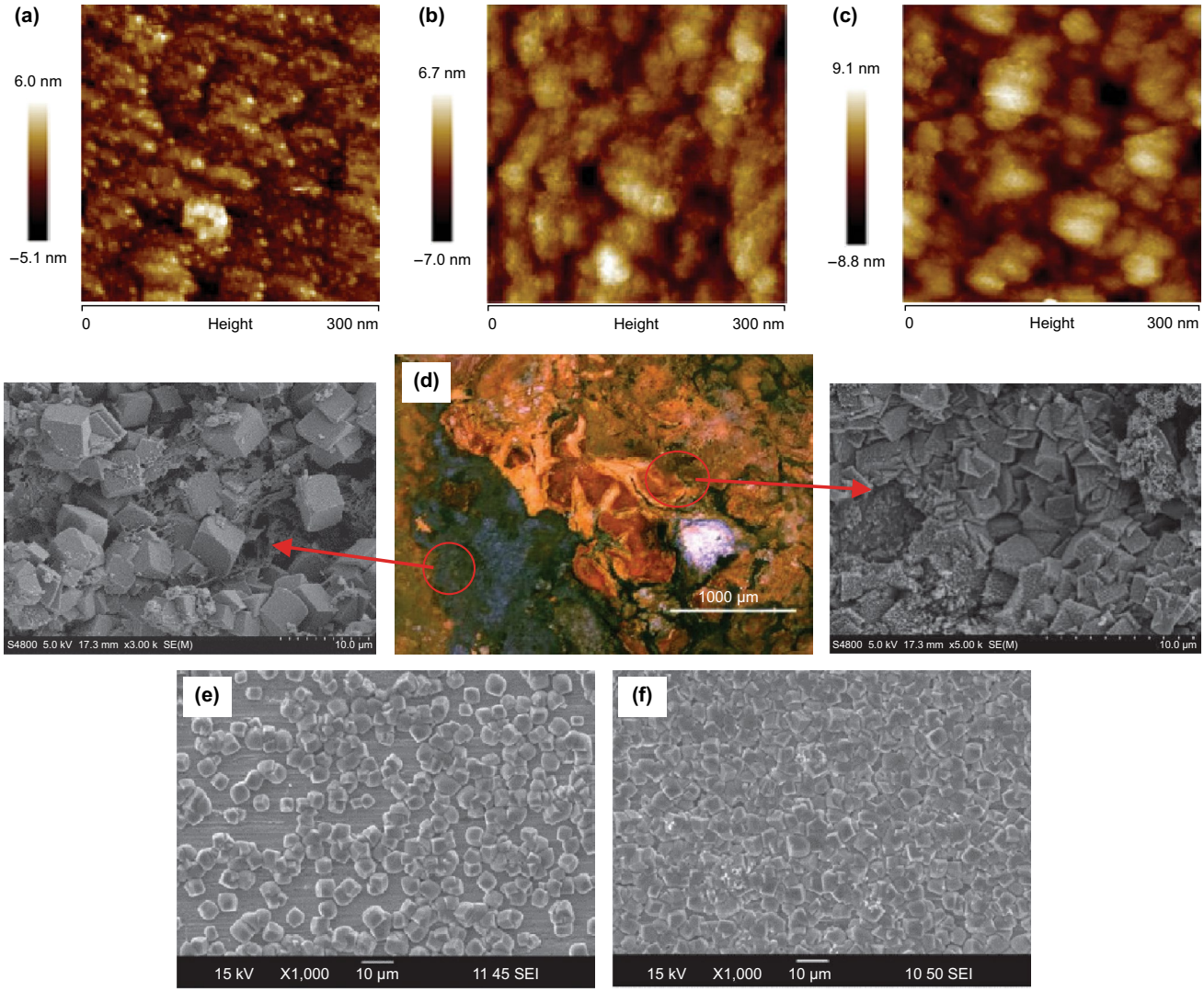


**Fig. 4** Changes of surface corrosion products of X80 steel with time at $i = 100$ A/m$^2$

of corrosion-product layer increased. At the same time, in the scope of 100 nm based on AFM, the inner layer was basically covered with the whole surface. The phenomenon was given elucidate in 10 μm range from SEM (Fig. 4e). At this time, corrosion products were scattered on the surface of the test piece disorderly, and covered the entire surface. Due to the coverage of corrosion products, $I_{corr}$ and $E_{corr}$ of X80 steel decreased, obtained by the Tafel polarization curves in Fig. 3. For another aspect, due to the incomplete coverage, there was no obvious passivation zone. After 1 h of immersion, the complete layer was formed, as shown in Fig. 4f.

(a), (b) and (c) were the AFM figures of inner corrosion-product layer after 10 min, 20 min and 30 min, respectively; (d) was the figure after 30 min, showing the structure of the double layer; (e) and (f) were the SEM figure for inner layer after 30 min and 1 h.

Based on the above analysis of morphology, the complete covered layer of $Fe_3O_4$ was come into being on X80 surface after 1 h at $i = 100$ A/m$^2$. Therefore, Fig. 5 expresses the potentiodynamic polarization curve, in which obvious passivation zone can be observed.

When immersion experiment at $i = 100$ A/m$^2$ lasted to 1 h, the $E_{corr} = -125.9$ mV, which was about equal to that in 30 min ($E_{corr\text{-}30min} = -122.3$ mV), indicating that in the time of 0.5–1 h, the process of forming inner layer took place. There were four typical points in passivation zone, named as $E_1$–$E_4$. Generally, in $E_{corr} - E_1$, corrosion behavior met with the Tafel's law, illustrating $Fe \rightarrow Fe^{2+} + 2e^-$ (Dillmann et al. 2002; Eliyan et al. 2012).

Firstly, as polarization potential rose up to $E_1$, the passivation occurred, in which (passivation potential) $E_p = E_1 = -99.2$ mV and (passivation current density) $I_{max} = 51.7$ A/m$^2$.

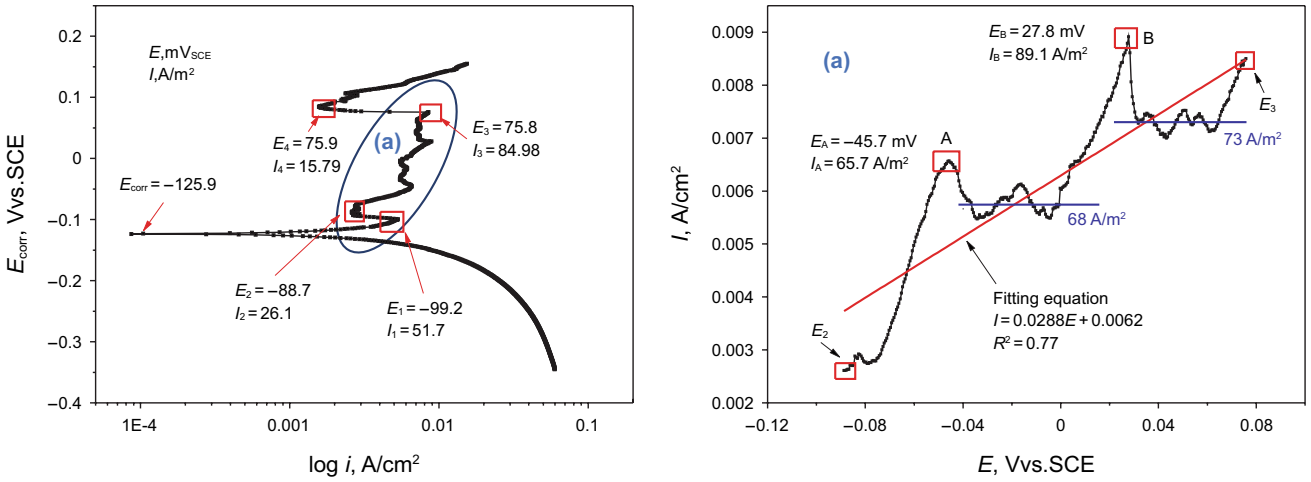


**Fig. 5** Polarization curve of X80 steel after 1 h at $i = 100 A/m^2$

Secondly, though the change of potential was little ($\Delta E = E_2 - E_1 = 10.5$ mV), the $I_1 = 51.7 A/m^2$ decreased to $I_2 = 26.1$ A/m$^2$, suggesting that the characteristic of the surface may be changed due to the formation of $(FeOH)_{ad}$ ($Fe + H_2O \leftrightharpoons (FeOH)_{ad} + H^+ + e^-$). At this time, the $E_2$ was also called activation or Flade potential ($E_F$).

Thirdly, in $E_2$–$E_3$, the $E$–$I$ curve showed a linear relationship, representing that $I_2 = 26.1$ A/m$^2$ increased to $I_3 = 84.98$ A/m$^2$, which was different from the passivation theory with the smallest anodic current. In this region, the $E$-$I$ curve was divided into three parts by point A ($E_A = -45.7$ mV, $I_A = 65.7$ A/m$^2$) and point B ($E_B = 27.8$ mV, $I_B = 89.1$ A/m$^2$). In $E_2 - E_A$, the anodic current linearly increased as potential enlarged, indicating that the adsorbed $(FeOH)_{ad}$ was reactivated to generate $Fe^{2+}$ [$(FeOH)_{ad} \rightarrow FeOH^+ + e^-$, $FeOH^+ + H + \leftrightharpoons Fe^{2+} + H_2O$). In $E_A$-$E_B$ and $E_B$-$E_3$, there were two steps, respectively, proving two difference electrochemical reaction: in $2Fe^{2+} + O_2 + 2H_2O \rightarrow 2FeO(OH) + 2H^+$ in $E_A$-$E_B$ and $FeO(OH) + Fe^{2+} + 2OH^- \rightarrow Fe_3O_4 + 2H_2O$ in $E_B$-$E_3$ (Tamaura et al. 1983).

Finally, from $E_3$ to $E_4$, there was only 0.1 mV increase with the 440% decrease of anodic current, which may be caused by the second polarization due to $I_3 = 84.98$ A/m$^2 \approx i = 100$ A/m$^2$. However, because of the high potential and conductivity of $Fe_3O_4$, the inner layer was easily broken down to activate corrosion. Therefore, the (over-passivation potential) $E_{tr} = E_4 = 75.9$ mV.

## 3.4 EIS measurements

In this paper, the electrochemical impedance spectrum (EIS) was used to investigate the passivation process of X80 steel in 3 wt% $NaHCO_3$ solution. The Nyquist plots and Bode diagrams were derived from the EIS measurements, and they were employed to interpret the role on corrosion behavior of the steel.

Figure 6 presents the Nyquist plots of the X80 steel affected by anodic current density exposed to the 3 wt% $NaHCO_3$ solution, and the fitted parameters are shown in Table 2.

To our best knowledge, in alkaline or near-neutral solution, the cathodic and anodic reaction of steel (Wang et al. 2019) can be described by $O_2 + 2H_2O + 4e^- \rightarrow 4OH^-$ and $Fe \rightarrow Fe^{2+} + 2e^-$, respectively. Therefore, the corrosion-product layer of $Fe^{2+} + 2OH^- \rightarrow Fe(OH)_2$ was formed without anodic current. Due to the porosity of $Fe(OH)_2$, the diffusion of corrosion product from the surface of steel to solution occurred, indicating the non-standard Warburg impendence in curve at $i = 0$. Considering the dispersion effect (Qiu et al. 2017; Hoseinieh et al. 2016), the pure capacitance of $C$ was replaced by constant phase angle element of $Q$; therefore,

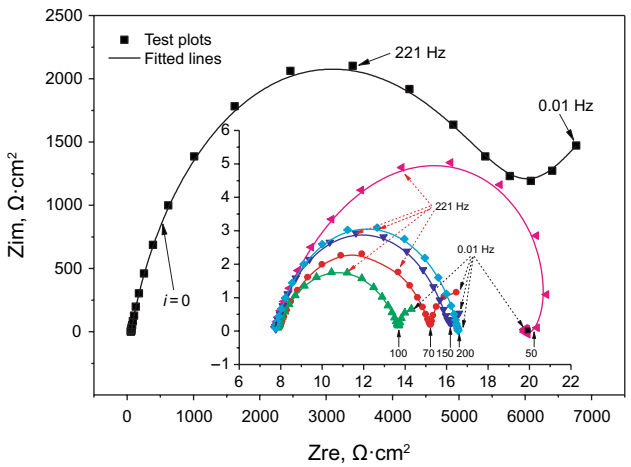


**Fig. 6** Nyquist plots of X80 steel at $i = 0$–$200$ A/m$^2$

**Table 2** Fitted parameters of EIS curves at different anodic current densities

| *i*-ACD parameter | 0 | 50 A/m$^2$ | 70 A/m$^2$ | 100 A/m$^2$ | 150 A/m$^2$ | 200 A/m$^2$ |
|---|---|---|---|---|---|---|
| $R_s$, Ω·cm$^2$ | 59.01 ± 1.19 | 7.66 ± 0.12 | 7.91 ± 0.09 | 8.66 ± 0.03 | 9.24 ± 0.07 | 9.73 ± 0.10 |
| $Q_{dl}$, $10^{-3}$ F/cm$^2$ | 5.60 ± 0.29 × $10^{-2}$ | 1.73 ± 0.42 | 1.32 ± 0.24 | 2.75 ± 0.31 | 1.70 ± 0.20 | 1.92 ± 0.28 |
| $n$ | 0.79 ± 0.01 | 0.71 ± 0.04 | 0.73 ± 0.03 | 0.69 ± 0.02 | 0.78 ± 0.02 | 0.78 ± 0.03 |
| $R_{ct}$, Ω·cm$^2$ | 5661 ± 222 | 16.73 ± 0.54 | 7.17 ± 0.18 | 5.86 ± 0.10 | 8.35 ± 0.16 | 8.83 ± 0.18 |
| $W$, Ω·cm$^2$ | 2.27 ± 0.29 × $10^{-3}$ | – | – | – | 5.41 ± 1.99 | – |
| $L$, H·cm$^2$ | – | 2.22 ± 0.93 | – | – | – | – |
| $R_0$, Ω·cm$^2$ | – | 45.80 ± 10.23 | – | – | – | – |
| $O$, F/cm$^2$ | – | – | 4.93 ± 1.24 | 5.33 ± 0.91 | – | – |
| $B$ | – | – | 3.17 ± 0.53 | 7.29 ± 1.64 | – | – |
| Error, $10^{-4}$ | 1.03 | 9.88 | 4.25 | 7.68 | 5.14 | 8.67 |

the equivalent electric circuit (EEC) can be described by $R_s(Q_{dl}(R_{ct}W))$: $R_s$ as solution resistance, $Q_{dl}$ as electrical double-layer capacitance, $R_{ct}$ as charge transfer resistance and $W$ as Warburg impendence.

As anodic current density increased, more and more corrosion products were quickly generated. In these cases, the surface condition of the X80 steel affected by $i = 50 \sim 200$ A/m$^2$ was controlled by two state parameters, named as anodic current density (*i*-ACD) and coverage rate of corrosion product on surface, respectively, indicating that the feature of Nyquist plots or corrosion current density was simultaneously demanded by these two state parameters. At $i = 50$ A/m$^2$, the $I_{corr}$ was larger than that of $i = 0$, resulted by the damage of intact film of $Fe(OH)_2$, indicating formation of local corrosion galvanic cells. Therefore, both of above two state parameters all made the $I_{corr}$ larger, and furthermore, the coverage rate was considered as the function of *i*-ACD, which resulted in the appearance of inductance feature. Therefore, the EEC was chosen as $R_s(Q_{dl}R_{ct}(LR_0))$ (Cao 2008): $L$ as inductance and $R_0$ as equivalent resistance of inductance.

From the analysis of Sect. 3.3, under the interference of anodic current, the corrosion product of X80 steel in $NaHCO_3$ solution changed from $Fe(OH)_2$ to FeO(OH) (Pérez et al. 2010). The α-FeO(OH) with a porous structure forming a relatively stable block structure affected the activity of corrosive medium under the porous film. For another aspect, γ-FeO(OH) with a higher cathode reactivity promoted the cathodic reaction process to accelerate the alkalinization under the porous film, facilitating the formation of $Fe_3O_4$. Therefore, at $i = 70$A/m$^2$, a dense layer of $Fe_3O_4$ under FeO(OH) layer was gradually formed. By this time, the double-layer structure has been come into being, even though the $Fe_3O_4$ layer was not sufficient to cover the entire steel surface due to the lower anodic current. At $i = 100$A/m$^2$, the inner $Fe_3O_4$ layer completely covered electrode surface, which can be proved by Fig. 5 with an obvious anode passivation area. Meanwhile, it can be found from the Nyquist plots of $i = 70$ A/m$^2$ and $i = 100$ A/m$^2$ that incomplete characteristics of "finite-layer diffusion" appeared in the tail of the reactance arc, which were also caused by the adsorption of the dense corrosion product $Fe_3O_4$ and its conductivity (Stratmann et al. 1987). Therefore, the EECs were $R_s(Q_{dl}(R_{ct}O))$ (Zhu et al. 2011): $O$ as finite-layer diffusion resistance.

As anodic current continually increased to 150 A/m$^2$, the electric field force between the working electrode and the auxiliary electrode was strong enough to compel the $Fe_3O_4$ layer damaged, leading to the occurrence of local defect of dense inner layer, which will accelerate the corrosion process of metallic matrix, making the concentration of ion near the steel larger than that in solution; therefore, the Warburg resistance was chosen to describe the EEC of $R_s(Q_{dl}(R_{ct}W))$. However, at $i = 200$ A/m$^2$, directional movement velocity of corrosion product or $Fe^{2+}$ from the surface of WE to solution was accelerated under the lager electric field force, causing little products lying on the surface. Therefore, the Nyquist plot showed a complete capacitive arc resistance and the EEC was $R_s(Q_{dl}R_{ct})$.

Moreover, the fitted data shown in Table 2 extracted from the EECs under different conditions of *i*-ACD showed that the charge transfer resistance of $R_{ct}$ was in a slight difference at $i = 50$–$200$ A/m$^2$. In general, a lower $R_{ct}$ illustrated a better resistance for corrosion, for example, $R_{ct} = 5661$ Ω·cm$^2$ at $i = 0$, which meant a lower reaction rate of $Fe \rightarrow Fe^{2+} + 2e^-$ compared with the others at $i = 50 \sim 200$ A/m$^2$. However, under this circumstance, the composition of passivation film was $Fe_3O_4$, showing a better electrical conductivity than the other Fe compound. As a consequence, a dense and integrated $Fe_3O_4$ layer had formed at $i = 100$ A/m$^2$, with a smallest charge transfer resistance of $R_{ct} = 5.86$ Ω·cm$^2$.

The other parameter reflecting the surface state was capacitance ($Q$), which represented mostly the same value. Based on the equation of $Q = \varepsilon_0 \varepsilon A/l$, the thickness of corrosion products at $i = 50$–$200$ A/m$^2$ can be regarded as keeping

unchanged. ($Q$ was the capacitance of the entire electrode system, including metal matrix and corrosion product; $\varepsilon_0$ and $\varepsilon$ was permittivity of vacuum and product film, respectively; $A$ was the surface area of X80 steel and $l$ was the total thickness of the corrosion product layer.)

Therefore, the position of activated ion in product film can be acquired by the definition of cathodic- and anodic-Tafel slop in analysis on polarization curves:

$$\beta_a = \frac{RT}{\alpha nF}, \quad \beta_c = \frac{RT}{(1-\alpha)nF} \tag{1}$$

where $\beta_a$ and $\beta_c$ is the anodic- and cathodic-Tafel slope, respectively; $R$ is the gas constant; $T$ is temperature; $nF$ is the charge of the activated ion; $\alpha$ is the reaction position of the activated ions ($Fe^{2+}$) in the double electric layer/corrosion product layer, and when $\alpha \to 0$, the activated ions are located on the surface of the metal matrix.

Combine $r = \beta_a/\beta_c$:

$$\alpha = \frac{1}{1+r} = \frac{1}{1+\beta_a/\beta_c} \tag{2}$$

According to fitting data of the Tafel slope in Table 2, $\alpha_{i=100} = 0.70$ and $\alpha_{i=200} = 0.08$, while $\alpha = 0.40 \sim 0.45$ at $i = 50$, 70 and 150 A/m$^2$. It can be seen from the above analysis that at $i = 50$, 70 and 150 A/m$^2$, the reaction position of activated ions remained basically unchanged when the inner membrane was in the process of formation or destruction. While at $i = 100$ A/m$^2$, the reaction position was close to the solution, and at $i = 200$A/m$^2$, the activated ion was nearly located on the surface of the electrode. This was consistent with the analysis of Nyquist plots.

Figure 7 shows the relationship of frequency-phase angle and frequency impedance. Under different anodic current conditions, the peak of phase angle ($\varphi$) occurred

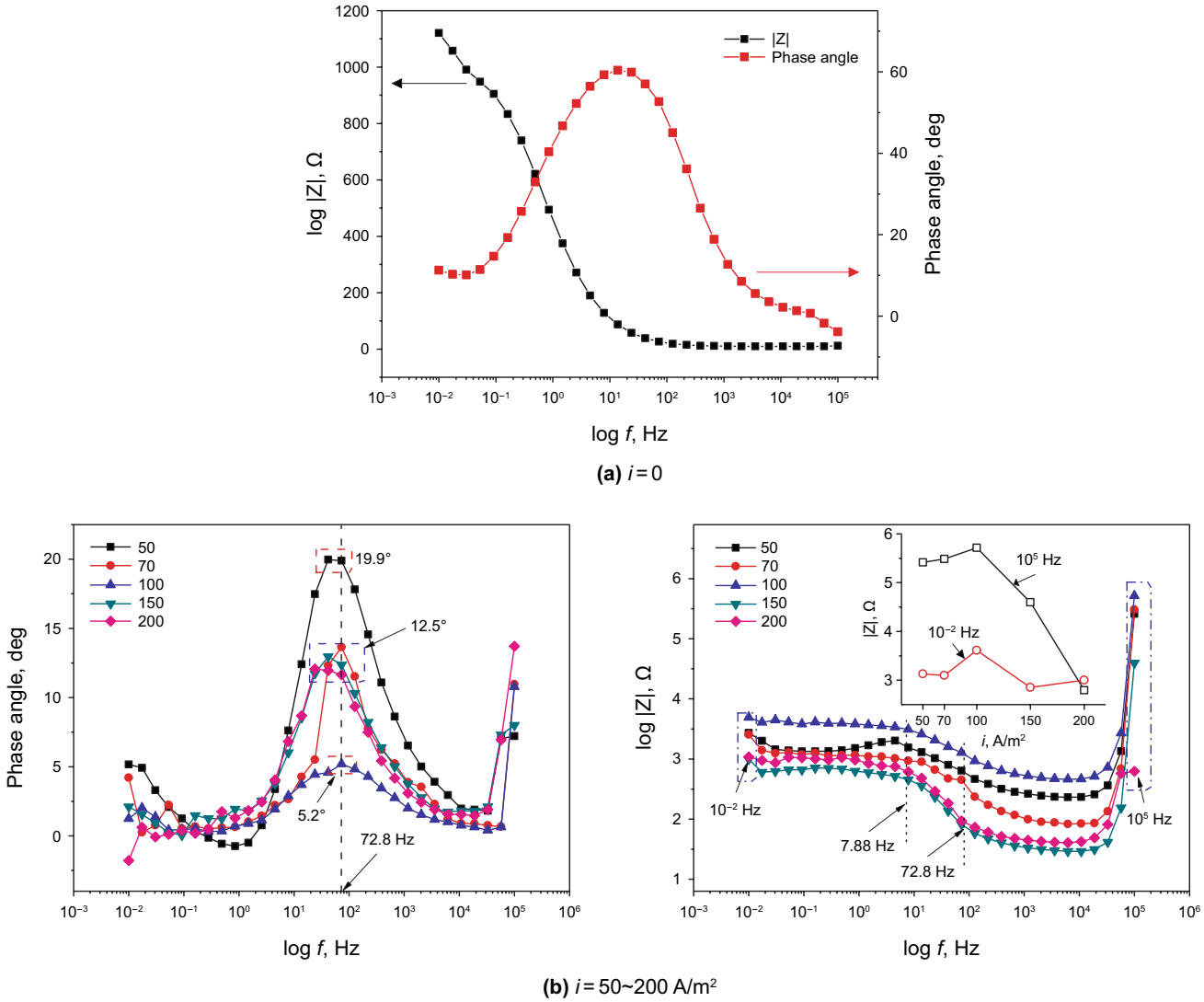


**Fig. 7** Diagrams of $f$-$\varphi$ and log$f$-|Z| of X80 steel at $i = 0$–200 A/m$^2$

at $f = 72.8$ Hz. Generally speaking, the ideal phase angle for a passivation system was − 90°, suggesting a pure non-conductive capacitor (Oliveira and Ferreira 2003). However, because the corrosion products of X80 steel had good electrical conductivity, the phase angle was far smaller than -90°, which can be identified as the characteristic of "resistance."

The change of maximal phase angle was consistent with variation in charge transfer resistance extracted from Nyquist plots. At $i = 50$ A/m$^2$, $\varphi = 19.9°$, and as $i$-ACD increased, the phase angle firstly decreased and then increased, indicating the minimum of $\varphi = 5.2°$ at $i = 100$ A/m$^2$. This was due to a better electric conductivity of $Fe_3O_4$, so as to closer to the resistance characteristics with a smallest phase angle.

As can be seen from the log$f$-log|Z| diagrams of the electrode system, it can be divided into three stages: $f = 10^{-2}$~7.88 Hz, $f = 7.88 \sim 72.8$ Hz and $f = 72.8 \sim 10^5$ Hz. The whole test system was presented as RC circuit with only one time constant, which was the same as the result of analysis on EECs. It can be seen that the mass transfer impedance at low frequency remained basically unchanged, while the charge transfer impedance at high frequency decreased with the increase of $i$-ACD. At the same time, there was only a small range representing the capacitor of corrosion product layer of $f = 7.88 \sim 72.8$ Hz, and the maximal phase angle appeared at $f = 72.8$ Hz, not moving to low frequency region with the change of $i$-ACD.

Therefore, the anodic current mainly affected the charge transfer process, while the entire electrode system was mainly characterized by resistance. Both the mass- and the charge-transfer resistance reached the maximum at $i = 100$ A/m$^2$, reflecting the formation of dense corrosion product layer of $Fe_3O_4$.

## 4 Conclusion

This paper focuses on the product and formation process of passivation film. The anodic passivation of X80 steel in 3 wt% $NaHCO_3$ solution occurred at $i = 100$ A/m$^2$ with two following conclusions:

(1) A dense and complete passivation film formed after 1 h at $i = 100$ A/m$^2$, in which there was a double-layer structure with FeO(OH) in outer and $Fe_3O_4$ in inner.
(2) The formation mechanism of $Fe_3O_4$ can be divided into two steps, which can be demonstrated by $2Fe^{2+} + O_2 + 2H_2O \rightarrow 2FeO(OH) + 2H^+$ in − 45.7~27.8 mV and $FeO(OH) + Fe^{2+} + 2OH^- \rightarrow Fe_3O_4 + 2H_2O$ in 27.8~75.8 mV.



## References

Cao CN. Corrosion electrochemical principle. Beijing: Chemical Industry Press; 2008 **(in Chinese)**.

Chen Z, Koleva D, van Breugel K. A review on stray current-induced steel corrosion in infrastructure. Corros Rev. 2017;35(6):397–423. https://doi.org/10.1515/corrrev-2017-0009.

Cui CL, Lim ATO, Huang JX. A cautionary note on graphene anti-corrosion coatings. Nat Nanotechnol. 2017;2(9):834–5. https://doi.org/10.1038/nnano.2017.187.

Cui ZY, Chen SS, Dou YP, et al. Passivation behavior and surface chemistry of 2507 super duplex stainless steel in artificial seawater: influence of dissolved oxygen and pH. Corros Sci. 2019;150:218–34. https://doi.org/10.1016/j.corsci.2019.02.002.

Dillmann P, Balasubramaniam R, Beranger G. Characterization of protective rust on ancient Indian iron using microprobe analyses. Corros Sci. 2002;44:2231–42. https://doi.org/10.1016/S0010-938X(02)00028-8.

Ejaz A, Lu ZP, Chen JJ, et al. The effect of hydrogen on anodic dissolution and passivation of iron in alkaline solutions. Corros Sci. 2015;10:165–81. https://doi.org/10.1016/j.corsci.2015.09.013.

Eliyan FF, Mahdi ES, Alfantazi A. Electrochemical evaluation of the corrosion behaviour of API-X100 pipeline steel in aerated bicarbonate solutions. Corros Sci. 2012;58:181–91. https://doi.org/10.1016/j.corsci.2012.01.015.

Hoseinieh SM, Homborg AM, Shahrabi T, et al. A novel approach for the evaluation of under deposit corrosion in marine environments using combined analysis by electrochemical impedance spectroscopy and electrochemical noise. Electrochim Acta. 2016;217:226–41. https://doi.org/10.1016/j.electacta.2016.08.146.

Jadhav N, Gelling VJ. Review-The use of localized electrochemical techniques for corrosion studies. J Electrochem Soc. 2019;116(11):C3461–76. https://doi.org/10.1149/2.0541911jes.

Li XG, Zhang DW, Liu ZY, et al. Materials science: share corrosion data. Nature. 2015;527(7579):441–2. https://doi.org/10.1038/527441a.

Liang YJ, Wang LJ, Wen YR, et al. High-content ductile coherent nanoprecipitates achieve ultrastrong high-entropy alloys. Nature Communications. 2018;9:4063. https://doi.org/10.1038/s41467-018-06600-8.

Nicholson P. High voltage direct current interference with underground or underwater pipelines. Houston: NACE International; 2010. p. 10102.

Oliveira CG, Ferreira MGS. Ranking high-quality paint systems using EIS. Part I: Intact coatings. Corrosion Science. 2003;45:123–38. https://doi.org/10.1016/S0010-938X(02)00088-4.

Pérez FR, Barrero CA, García KE. Factors affecting the amount of corroded iron converted into adherent rust in steels submitted to immersion tests. Corros Sci. 2010;52:2582–91. https://doi.org/10.1016/j.corsci.2010.04.005.

Philippe LVS, Lyon SB, Sammon C, et al. Validation of electrochemical impedance measurements for water sorption into epoxy

coatings using gravimetry and infra-red spectroscopy. Corros Sci. 2008;50:887–96. https://doi.org/10.1016/j.corsci.2007.09.008.

Prasai D, Tuberquia JC, Harl RR, et al. Graphene: corrosion-inhibiting coating. ACS Nano. 2012;6(2):1102–8. https://doi.org/10.1021/nn203507y.

Qiu SH, Li W, Zheng WR, et al. Synergistic effect of polypyrrole-intercalated graphene for enhanced corrosion protection of aqueous coating in 3.5% NaCl solution. ACS Appl Mater Interfaces. 2017;9:34294–304. https://doi.org/10.1021/acsami.7b08325.

Raman A, Nasrazadani S, Sharma L. Morphology of rust phases formed on weathering steels in various laboratory corrosion tests. Metallography. 1989;22:79–96. https://doi.org/10.1016/0026-0800(89)90024-4.

Refait Ph, Jeannin M, Sabot R, et al. Corrosion and cathodic protection of carbon steel in the tidal zone: products, mechanisms and kinetics. Corros Sci. 2015;90:375–82. https://doi.org/10.1016/j.corsci.2014.10.035.

Stratmann M, Bohnenkamp K, Ramchandran T. The influence of copper upon the atmospheric corrosion of iron. Corros Sci. 1987;27:905–26. https://doi.org/10.1016/0010-938X(87)90058-8.

Tamaura Y, Ito K, Katsura T. Transformation of γ-FeO(OH) to $Fe_3O_4$ by adsorption of iron(II) ion on γ-FeO(OH). J Chem Soc Dalton Trans. 1983;2:189–94.

Tanaka H, Mishima R, Hatanaka N, et al. Formation of magnetite rust particles by reacting iron powder with artificial α-, β- and γ-FeO(OH) in aqueous media. Corros Sci. 2014;78:384–7. https://doi.org/10.1016/j.corsci.2013.08.023.

Tranchida G, Clesi M, Di Franco F, et al. Electronic properties and corrosion resistance of passive film on austenitic and duplex stainless steels. Electrochim Acta. 2018;273:412–23. https://doi.org/10.1016/j.electacta.2018.04.058.

Wang DY, Zhu ZW, Wang NF, et al. Investigation of the electrochemical dissolution behavior of Inconel 718 and 304 stainless steel at low current density in $NaNO_3$ solution. Electrochim Acta. 2015;156:301–7. https://doi.org/10.1016/j.electacta.2014.12.155.

Wang LW, Xin JC, Cheng LJ, et al. Influence of inclusions on initiation of pitting corrosion and stress corrosion cracking of X70 steel in near-neutral pH environment. Corros Sci. 2019;147:108–27. https://doi.org/10.1016/j.corsci.2018.11.007.

Xu LY, Su X, Yin ZX, et al. Development of a real-time AC/DC data acquisition technique for studies of AC corrosion of pipelines. Corros Sci. 2012;61:215–23. https://doi.org/10.1016/j.corsci.2012.04.038.

Xu WQ, Birbilis N, Sha G, et al. A high-specific-strength and corrosion-resistant magnesium alloy. Nat Mater. 2015;14:1229–36. https://doi.org/10.1038/nmat4435.

Yang C, Li JL, Li ZL, et al. Study on interference and protection of pipeline due to high-voltage direct current electrode. Corros Rev. 2019;37(3):273–81. https://doi.org/10.1515/corrrev-2018-0089.

Zhang Y, Tian JW, Zhong J, et al. Thin nacre-biomimetic coating with super-anticorrosion performance. ACS Nano. 2018;12:10189–200. https://doi.org/10.1021/acsnano.8b05183.

Zhu CF, Xie R, Xue JH, et al. Studies of the impedance models and water transport behaviors of cathodically polarized coating. Electrochim Acta. 2011;56:5828–35. https://doi.org/10.1016/j.electacta.2011.04.068.